



Multicomponent Transition Metal Dichalcogenide Nanosheets for Imaging-Guided Photothermal and Chemodynamic Therapy

Yu Zhu, Yingjie Wang, Gareth R. Williams, Liyang Fu, Jingjing Wu, Hui Wang, Ruizheng Liang,* Xisheng Weng,* and Min Wei*

Transition metal dichalcogenides (TMDs) have received considerable attention due to their strong absorption in the near-infrared (NIR) region, strong spin-orbit coupling, and excellent photothermal conversion efficiency (PCE). Herein, CoFeMn dichalcogenide nanosheets (CFMS NSs) are prepared via facile vulcanization of a lamellar CoFeMn-layered double hydroxide (LDH) precursor followed by polyvinyl pyrrolidone modification (to give CFMS-PVP NSs), and found to show excellent photoacoustic (PA) imaging and synergistic photothermal/chemodynamic therapy (PTT/CDT) performance. The as-prepared CFMS-PVP NSs inherit the ultrathin morphology of the CoFeMn-LDH precursor and exhibit an outstanding photothermal performance with a η of 89.0%, the highest PCE reported to date for 2D TMD materials. Moreover, 50% of maximum catalytic activity (Michaelis–Menten constant, K_m) is attained by CFMS-PVP NSs with 0.26×10^{-3} M H_2O_2 at 318 K, markedly lower than the endogenous concentration of H_2O_2 inside tumor cells. In addition, complete apoptosis of HepG2 cancer cells and complete tumor elimination in vivo are observed after treatment with CFMS-PVP NSs at a low dose, substantiating the NSs' remarkable PTT/CDT efficacy. This work provides a new and facile approach for the synthesis of high-quality multicomponent TMD nanosheets with precise process control, the potential for mass production, and outstanding performance, providing great promise in cancer theranostics.

1. Introduction

Transition metal dichalcogenides (TMDs) have received considerable attention due to their tunable bandgaps, strong spin-orbit coupling, and excellent optical and thermal conversion efficiency.^[1] For example, MoS_2 , WS_2 , and $NiTe_2$ show strong absorption in the near-infrared (NIR) region, which makes them ideal photoacoustic (PA) imaging contrast agents and photothermal therapy (PTT) agents.^[2] In order to achieve suitable photothermal therapeutic performance, the key factor is to fabricate high-efficiency photothermal agents. In contrast to the multilayer structure of bulk TMDs, ultrathin TMD nanosheets possess a higher photothermal conversion efficiency (PCE) due to the change of band structure.^[3] Moreover, compared with mono- and dual-metal TMD NSs, the high entropy induced by multi-metal coordination endows TMD NSs with tunable and enhanced intrinsic optical and electronic properties, which is of benefit for PTT efficiency.^[4] Nevertheless, it is still difficult to completely eradicate deep tumors and prevent metastasis by PTT

Y. Zhu, L. Fu, J. Wu, H. Wang, Dr. R. Liang, Prof. M. Wei
State Key Laboratory of Chemical Resource Engineering
Beijing Advanced Innovation Center for Soft Matter Science and
Engineering
Beijing University of Chemical Technology
Beijing 100029, P. R. China
E-mail: liangrz@mail.buct.edu.cn; weimin@mail.buct.edu.cn

Y. Wang, Prof. X. Weng
Department of Orthopaedics
Peking Union Medical College Hospital
Peking Union Medical College & Chinese Academy of Medical Sciences
Beijing 100730, P. R. China
E-mail: xshweng@medmail.com.cn
Dr. G. R. Williams
UCL School of Pharmacy
University College London
29-39 Brunswick Square, London WC1N 1AX, UK

The ORCID identification number(s) for the author(s) of this article can be found under <https://doi.org/10.1002/adv.202000272>

© 2020 The Authors. Published by WILEY-VCH Verlag GmbH & Co. KGaA, Weinheim. This is an open access article under the terms of the Creative Commons Attribution License, which permits use, distribution and reproduction in any medium, provided the original work is properly cited.

DOI: 10.1002/adv.202000272

alone, due to the fact that heat dispersion within the solid tumor is inhomogeneous and because of the depth-dependent decline of laser intensity upon external irradiation.^[5] Therefore, modulating composition and structure to increase PTT effectiveness, and combining PTT with other therapeutic modalities, are vital to fulfill their potential in cancer theranostics.

Chemodynamic therapy (CDT) utilizes the iron-initiated Fenton reaction or Fenton-like reactions mediated by other metal ions (such as Co^{2+} , Ti^{3+} , Ni^{2+} , Cu^{2+} , and Mn^{2+}) to specifically eliminate tumor cells by converting intracellular H_2O_2 into toxic hydroxyl radicals ($\cdot\text{OH}$) in acidic conditions. This surmounts issues of tumor nonspecificity and the toxicity of chemotherapeutic drugs.^[6] However, the fact that glutathione (GSH), which has $\cdot\text{OH}$ scavenging ability, is overexpressed in the tumor microenvironment and has restricted the application of CDT to some degree.^[7] Thus, the reduction of intracellular GSH level is highly desirable for potent CDT. Moreover, previous reports indicate that external energy fields such as heat could be explored to accelerate Fenton and Fenton-like reactions and increase CDT efficacy.^[8] The combination of PTT and CDT will result in effective synergistic cancer therapy, overcoming the inadequacies of any single therapy.^[9] Therefore, the preparation of TMDs containing photothermal and chemodynamic dual-functional metal species should allow construction of an “all in one” platform to realize imaging-guided PTT/CDT. However, there are few reports on multicomponent ultrathin TMDs for biomaterial applications, partly due to limitations in terms of preparation. In stark contrast to TMDs, layered double hydroxide (LDH) nanosheets can be synthesized with very high degrees of structural and compositional control, and at large scale.^[10] LDH nanosheets are thus widely explored 2D nanomaterials. Their chemical formula can be expressed as $[\text{M}^{2+}_{1-x}\text{M}^{3+}_x(\text{OH})_2](\text{A}^{n-})_{x/n} \cdot m\text{H}_2\text{O}$, where M^{2+} and M^{3+} are metal ions distributed in an edge-sharing MO_6 octahedral host layer.^[11] A topotactic transformation reaction can be envisaged which might allow the synthesis of ultrathin TMDs from an LDH precursor.^[12] The resulting TMD nanosheets would inherit the intrinsic architecture, structure and composition of the LDH precursor. Hence, the TMD's properties could be finely tuned through modulating the LDH precursor and transformation conditions.

Herein, polyvinyl pyrrolidone (PVP) modified CoFeMn dichalcogenide nanosheets (CFMS-PVP NSs) are prepared via facile vulcanization of a lamellar CoFeMn-LDH precursor for the first time, and show excellent PA imaging and PTT/CDT synergistic therapy performance. X-ray diffraction (XRD) patterns show the CFMS NSs to comprise a hybrid crystal structure of FeS_2 and CoS_2 , while transmission electron microscope (TEM) and atomic force microscope (AFM) images reveal ultrathin structures with an average size of ≈ 54.0 nm and a thickness of ≈ 1.2 nm. The PCE (η) of the CFMS-PVP NSs can reach 89.0% through modulation of the Co/Fe/Mn ratio in the LDH precursor, the highest PCE ever reported among 2D TMDs. The CFMS-PVP NSs could convert H_2O_2 in situ into toxic $\cdot\text{OH}$ via Fenton and Fenton-like reactions of Co^{2+} and $\text{Fe}^{2+}/\text{Fe}^{3+}$, with an ultralow Michaelis–Menten constant ($K_m = 0.26 \times 10^{-3}$ M at 318 K) while the $\text{Mn}^{4+}/\text{Mn}^{3+}$ in the CFMS-PVP NSs could consume GSH rapidly through a redox reaction. Moreover, the NSs have excellent PA imaging capabilities with an ultralow detection limit, as is demonstrated in vivo. Both in vitro and in

vivo tests (including conventional and in situ tumor models) substantiate remarkable PTT/CDT efficacy, with complete apoptosis of HepG2 cancer cells and complete tumor elimination after treatment with CFMS-PVP NSs.

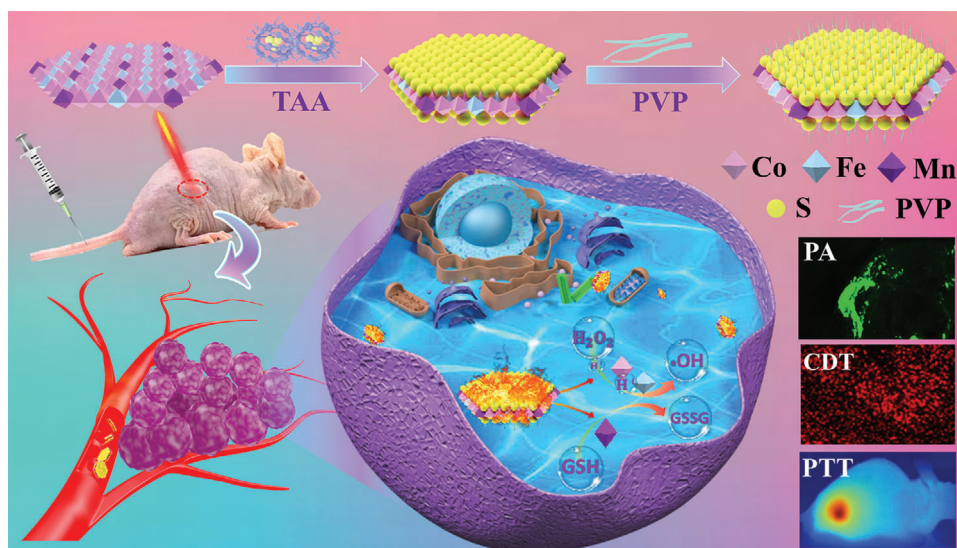
2. Result and Discussion

2.1. Synthesis and Characterization

The fabrication of the CFMS-PVP NSs is illustrated in **Scheme 1**. Lamellar CoFeMn-LDH precursors were first prepared by a “bottom-up” synthesis route, followed by a facile vulcanization process to obtain ultrathin CFMS NSs.^[13] The CoFeMn-LDH precursors have high crystallinity, as demonstrated by their XRD patterns (Figure S1, Supporting Information), which show a series of (00l) reflections. After vulcanization, the XRD patterns of the CFMS NSs (Figure S2, Supporting Information) display Bragg reflections which can be ascribed to cubic FeS_2 (JCPDS Card No. 42-1340) and CoS_2 structures (JCPDS Card No. 41-1471). A TEM image of the $\text{Co}_2\text{Fe}_{0.75}\text{Mn}_{0.25}$ -LDH precursor shows a monodispersed nanosheet morphology, with a lateral size of 50.0 ± 4.5 nm (**Figure 1A**). After vulcanization, the resulting CFMS NSs inherit the plate-like morphology and particle size of the precursor, with a diameter 54.0 ± 5.1 nm (**Figure 1B**). Energy-dispersive X-ray (EDX) mapping of the $\text{Co}_2\text{Fe}_{0.75}\text{Mn}_{0.25}$ -LDH precursor reveals a homogeneous distribution of Co, Fe, Mn, and O (**Figure 1C**), while a uniform dispersion of Co, Fe, Mn, and S is observed for the CFMS NSs (**Figure 1D**). Thus, it is proposed that CFMS NSs possess a $\text{CoS}_2/\text{FeS}_2$ crystal phase with Mn doping into the lattice. An AFM image of the $\text{Co}_2\text{Fe}_{0.75}\text{Mn}_{0.25}$ -LDH precursor gives a thickness of ≈ 1.1 nm (**Figure 1E,F**). This ultrathin structure is maintained after vulcanization, and the CFMS NSs have an unaltered thickness of ≈ 1.2 nm (**Figure 1G,H**).

In order to enhance dispersion stability and biocompatibility for further experimental studies, the surface of the $\text{Co}_2\text{Fe}_{0.75}\text{Mn}_{0.25}\text{S}_6$ NSs was functionalized with PVP. Fourier transform infrared spectroscopy (FT-IR) was performed to verify the synthesis of LDH precursor, CFMS NSs and CFMS-PVP NSs (**Figure 1I**). The LDH spectrum contains a broad band at 3420 cm^{-1} , corresponding to the stretching mode of hydroxyl groups. The broad intense band at around 1384 cm^{-1} is attributed to N–O vibrations of nitrate ions. The CFMS spectrum presents no nitrate bands, but instead M–S vibrations are visible in the low wavelength region. C–N stretching bands at 1423 and 1290 cm^{-1} are observed with CFMS-PVP NSs, which indicates PVP is successfully loaded onto the NSs.

X-ray photoelectron spectroscopy (XPS) was employed to characterize the chemical composition and valence state of the samples. For the $\text{Co}_2\text{Fe}_{0.75}\text{Mn}_{0.25}$ -LDH precursor (**Figure S3**, Supporting Information), peaks at 780.3 and 797.1 eV are assigned to Co^{2+} $2p_{3/2}$ and $2p_{1/2}$, peaks at 712.3 and 724.6 eV are attributed to Fe^{3+} $2p_{3/2}$ and $2p_{1/2}$, and peaks at 642.2 and 653.8 eV correspond to Mn^{4+} $2p_{3/2}$ and $2p_{1/2}$. After vulcanization (**Figure S4**, Supporting Information), the Co $2p_{3/2}$ and $2p_{1/2}$ binding energies of 779.5 and 794.2 eV are characteristic of CoS_2 . The Fe $2p_{3/2}$ peaks at 707.8 , 710.3 eV and Fe $2p_{1/2}$ band at 720.6 eV can be assigned to Fe^{2+} . The relative proportions of Fe^{2+} and Fe^{3+} were determined to be 67.2% and 32.8%. The peaks at 641.0 , 642.0 ,



Scheme 1. A schematic illustration for preparing CFMS-PVP NSs to give efficient PTT/CDT and PA imaging.

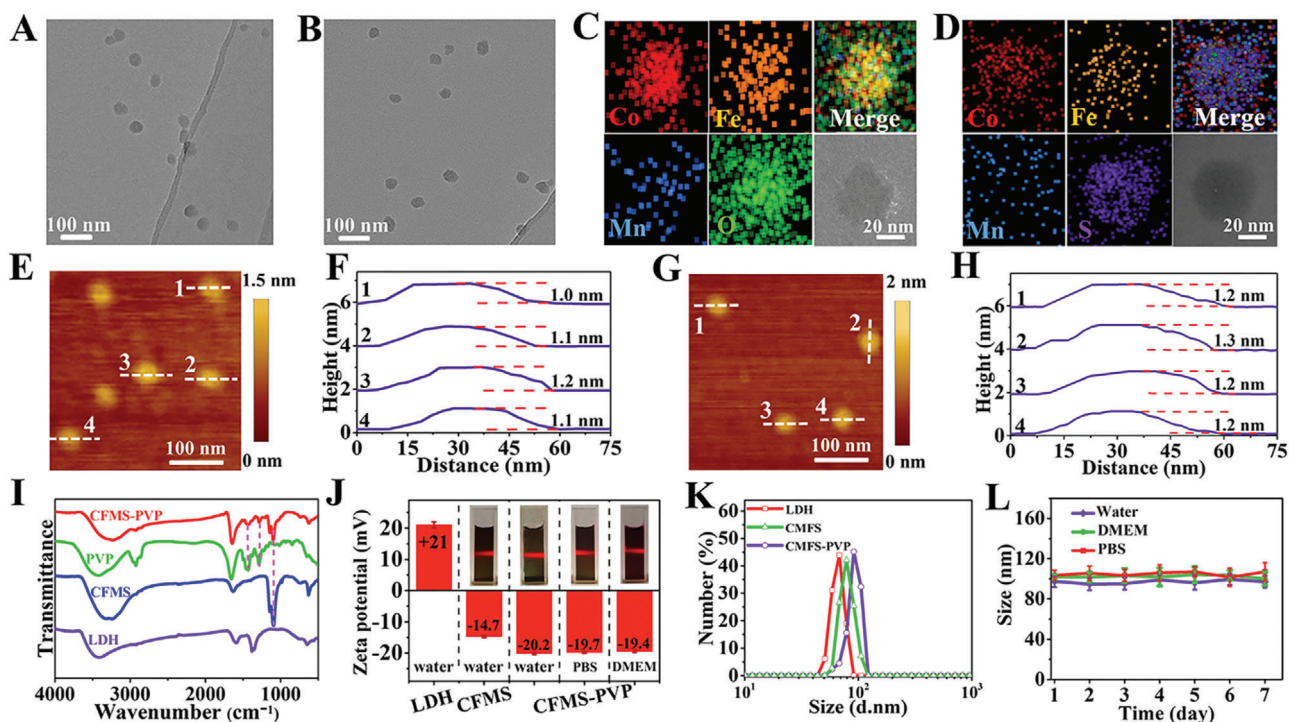


Figure 1. Structure and physicochemical properties of the $\text{Co}_2\text{Fe}_{0.75}\text{Mn}_{0.25}\text{-LDH}$ and $\text{Co}_2\text{Fe}_{0.75}\text{Mn}_{0.25}\text{S}_6$ samples. A, B) TEM images, C, D) EDX mapping, E–H) AFM images of $\text{Co}_2\text{Fe}_{0.75}\text{Mn}_{0.25}\text{-LDH}$ and $\text{Co}_2\text{Fe}_{0.75}\text{Mn}_{0.25}\text{S}_6$ NSs, respectively. I) FT-IR spectra. J) Zeta potential and K) size distributions. L) Particle sizes in water, PBS or DMEM for 7 days ($n = 3$, mean \pm S.D.).

and 644.0 eV are attributed to Mn^{2+} , Mn^{3+} and Mn^{4+} with proportions of 18.3%, 55.0%, and 26.7% respectively. In the S 2p region, the peaks at 162.6 and 163.9 eV are attributed to S^{2-} , while the minor peak at 167.9 eV can be ascribed to the presence of a small amount of SO_4^{2-} .

The physicochemical properties of the $\text{Co}_2\text{Fe}_{0.75}\text{Mn}_{0.25}\text{S}_6$ and $\text{Co}_2\text{Fe}_{0.75}\text{Mn}_{0.25}\text{S}_6\text{-PVP}$ NSs were further investigated. CFMS NSs show a negative zeta potential of -14.7 ± 0.2 mV in aqueous

suspension, in contrast to the positive potential of the LDH sample (21.0 ± 0.7 mV, Figure 1J). After PVP functionalization, the zeta potential of the CFMS-PVP NSs changed to -20.2 ± 0.3 mV, -19.7 ± 0.2 and -19.4 ± 0.1 mV in aqueous solution, phosphate buffer saline (PBS) and pure Dulbecco's Modified Eagle's Medium (DMEM). The CFMS-PVP NSs showed a lateral size of 57.0 ± 4.3 nm and a thickness of ≈ 3.2 nm (Figures S5 and S6, Supporting Information). Dynamic light scattering (DLS) data

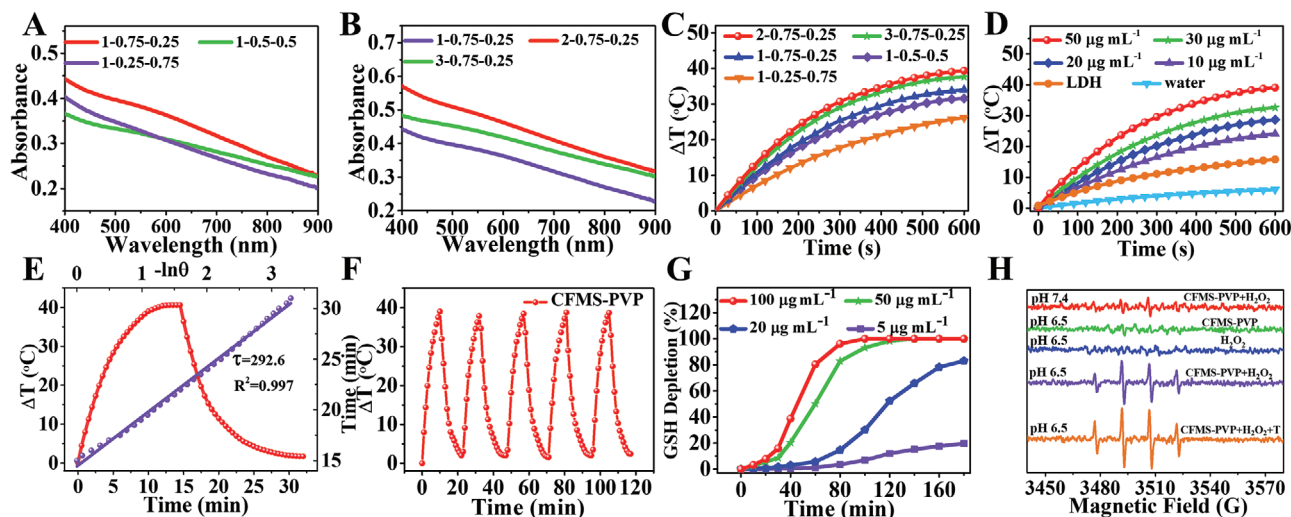


Figure 2. PTT and CDT performance. A,B) UV-vis absorbance spectra and C) photothermal heating curves of CFMS-PVP NSs with different ratios of Co: Fe: Mn. D) Temperature elevation of CFMS-PVP NS suspensions (Co: Fe: Mn = 2: 0.75: 0.25) at different concentration (0, 10, 20, 30, and 50 $\mu\text{g mL}^{-1}$) and the $\text{Co}_2\text{Fe}_{0.75}\text{Mn}_{0.25}$ -LDH precursor (50 $\mu\text{g mL}^{-1}$) upon 808 nm laser irradiation (1.0 W cm^{-2}). E) Calculation of the PCE at 808 nm. The time constant (τ_5) for the heat transfer was calculated from the cooling period (purple line). F) Temperature variation of $\text{Co}_2\text{Fe}_{0.75}\text{Mn}_{0.25}\text{S}_6$ -PVP NSs under irradiation at 1.0 W cm^{-2} for 5 on/off cycles (10 min irradiation for each cycle). G) GSH depletion under reduction by $\text{Co}_2\text{Fe}_{0.75}\text{Mn}_{0.25}\text{S}_6$ -PVP NSs. H) ESR spectra of $\text{Co}_2\text{Fe}_{0.75}\text{Mn}_{0.25}\text{S}_6$ -PVP NSs with H_2O_2 at different pH and temperatures (spectra of the NSs and H_2O_2 alone are shown as controls).

for CFMS-PVP NSs reveal the hydrodynamic particle size to be around $101.5 \pm 5.5 \text{ nm}$ in three different media (water, PBS, and DMEM), and there are no notable changes in particle diameter distribution over 7 days of storage (Figure 1K,L). An obvious Tyndall effect can be seen for CFMS-PVP NSs dispersed in water, DMEM and PBS during storage for 7 days (Figure S7, Supporting Information), which demonstrates their satisfactory storage stability and good dispersibility.

The morphology and size distributions of CFMS-PVP samples prepared from a range of different LDH precursors with varied metal ratios were also explored. TEM and DLS both show a lamellar morphology with hydrodynamic particle size of $\approx 100.0 \text{ nm}$ (Figure S8, Supporting Information). The materials are hence all similar in terms of particle size and shape regardless of the metal composition. The mass ratio of PVP in the final $\text{Co}_2\text{Fe}_{0.75}\text{Mn}_{0.25}\text{S}_6$ -PVP NSs was estimated to be 6.40% by thermogravimetry (Figure S9, Supporting Information).

2.2. Photothermal and Chemodynamic Properties of CFMS-PVP NSs

The influence of the Co/Fe/Mn molar ratio on the crystal structure and PTT performance of CFMS-PVP NSs was studied. Through altering the ratio of Fe/Mn (0.25: 0.75, 0.5: 0.5, and 0.75: 0.25) in the LDH precursor, with constant Co content, a series of TMDs could be obtained. The crystallinity of the CFMS NSs changes markedly, and a ratio of 0.75: 0.25 gives rise to the strongest reflection intensities in XRD (Figure S2A, Supporting Information). With an increased content of Co, metal-ligand charge transfers from Co 3d to S 4s orbitals and d-d transitions of Co will enhance absorption in the UV-vis region.^[14] However, when altering the ratio of Co (from 1 to 3) with constant Fe/Mn

(0.75: 0.25), the reflection intensity of the $\text{CoS}_2/\text{FeS}_2$ phase declines markedly (Figure S2B, Supporting Information), and only $\text{Co}_1\text{Fe}_{0.75}\text{Mn}_{0.25}\text{S}_4$ and $\text{Co}_2\text{Fe}_{0.75}\text{Mn}_{0.25}\text{S}_6$ retain the $\text{CoS}_2/\text{FeS}_2$ structure. The near-infrared (NIR) absorption of the various CFMS-PVP NSs ($\text{Co}_x\text{Fe}_y\text{Mn}_{1-y}\text{S}_{2(x+y)}$ -PVP) was recorded, and the $\text{Co}_2\text{Fe}_{0.75}\text{Mn}_{0.25}\text{S}_6$ -PVP sample showed the greatest absorbance at 808 nm (Figure 2A,B). Results from inductively coupled plasma (ICP) show that the molar ratio of Co/Fe/Mn in the CFMS products is close to the feed ratio (Table S1, Supporting Information).

Subsequently, the $\text{Co}_x\text{Fe}_y\text{Mn}_{1-y}\text{S}_{2(x+y)}$ -PVP samples were irradiated with an 808 nm laser at a power density of 1.0 W cm^{-2} , and the temperature changes were monitored. As shown in Figure 2C, $\text{Co}_2\text{Fe}_{0.75}\text{Mn}_{0.25}\text{S}_6$ -PVP NSs possess the best photothermal performance, which is consistent with the NIR absorption data. The photothermal performance of the $\text{Co}_2\text{Fe}_{0.75}\text{Mn}_{0.25}\text{S}_6$ -PVP NSs is strongly dependent on the concentration and the laser power: an increase in temperature (ΔT) ranging from 24.7 to 39.4 $^\circ\text{C}$ is obtained along with the increase of concentration (10–50 $\mu\text{g mL}^{-1}$, Figure 2D), and ΔT can be finely tuned from 9.7 to 39.4 $^\circ\text{C}$ by enhancing the laser power (0.25–1.0 W cm^{-2} , Figure S10, Supporting Information). A clear visual change in temperature can be seen for CFMS suspensions when using a thermal infrared imaging device (Figure S11, Supporting Information).

In contrast, control samples (PBS and CoFeMn-LDH suspension: 50 $\mu\text{g mL}^{-1}$) exposed to the NIR laser only give a temperature increment of 6.0 and 15.8 $^\circ\text{C}$, respectively. Notably, the PCE of $\text{Co}_2\text{Fe}_{0.75}\text{Mn}_{0.25}\text{S}_6$ -PVP NSs is determined to be 89.0% (Figure 2E), significantly greater than for previously reported 2D TMDs such as TaS_2 -PEG NSs (39.0%), Cu-Fe-Se NSs (78.9%), ReS_2 NSs (79.2%), etc. (Table S2, Supporting Information). We further compared the photothermal effect of $\text{Co}_2\text{Fe}_1\text{S}_6$ -PVP and the $\text{Co}_2\text{Fe}_{0.75}\text{Mn}_{0.25}\text{S}_6$ -PVP NSs. $\text{Co}_2\text{Fe}_1\text{S}_6$ -PVP NSs leads to an increase of 31.4 $^\circ\text{C}$ while CFMS-PVP NSs induces a 39.4 $^\circ\text{C}$

increment after 10 min irradiation at the power density of 1.0 W cm^{-2} . The PCE (η) values for $\text{Co}_2\text{Fe}_{0.75}\text{Mn}_{0.25}\text{S}_6$ -PVP and $\text{Co}_2\text{Fe}_1\text{S}_6$ -PVP NSs are 89.0% and 76.4% respectively (Figure S12, Supporting Information), demonstrating the superior photothermal performance of the CFMS-PVP NSs. The high PCE of the $\text{Co}_2\text{Fe}_{0.75}\text{Mn}_{0.25}\text{S}_6$ -PVP NSs can be attributed to the following factors. Firstly, the ultrathin 2D structure of the CFMS-PVP NSs endows them with a large surface area ($185.59 \text{ m}^2 \text{ g}^{-1}$; Figure S13, Supporting Information). This permits them to serve as laser-cavity mirrors with improved absorption of photoelectrons, leading the interaction time between the photoelectrons and the material being extended. Secondly, nanomaterials with smaller bandgaps possess higher PCE in comparison with those with wider bandgaps.^[15] The bandgap of the $\text{Co}_2\text{Fe}_{0.75}\text{Mn}_{0.25}\text{S}_6$ -PVP NSs was determined to be 0.57 eV, highly beneficial for PCE (Figure S14, Supporting Information). Thirdly, compared with two-metal materials, multi-metal coordination endows TMDs with an enhanced PCE. This is clear from a comparison of $\text{Co}_2\text{Fe}_1\text{S}_6$ -PVP and the $\text{Co}_2\text{Fe}_{0.75}\text{Mn}_{0.25}\text{S}_6$ -PVP NSs, where the latter show noticeably better photothermal performance (Figure S12, Supporting Information). In addition, no significant deterioration in performance can be detected after 5 successive heating-cooling cycles (Figure 2F), confirming the photothermal stability of the CFMS-PVP NSs.

Inspired by the excellent photothermal conversion properties of the $\text{Co}_2\text{Fe}_{0.75}\text{Mn}_{0.25}\text{S}_6$ -PVP NSs, their photoacoustic properties were evaluated.^[16] A significant enhancement of PA signal intensity is observed for CFMS-PVP NSs with an increase of sample concentration, with a linear correlation from 0 to $50 \mu\text{g mL}^{-1}$ (Figure S15, Supporting Information). The PA signal intensity from a suspension of the CFMS-PVP NSs was about 3.3 times higher than an LDH suspension at the same concentration, indicating a markedly enhanced PA performance after vulcanization.

GSH can react with the $\cdot\text{OH}$ generated in CDT, and oxidation of intracellular GSH to GSSG is highly beneficial for effective CDT treatment. We thus investigated the reaction between CFMS-PVP NSs and GSH. 5, 5-Dithiobis-(2-nitrobenzoic acid (DTNB) was used to detect GSH depletion after the addition of different concentrations of $\text{Co}_2\text{Fe}_{0.75}\text{Mn}_{0.25}\text{S}_6$ -PVP NSs.^[17] As shown in Figure 2G, significantly increased GSH depletion (from an initial concentration of $1.0 \times 10^{-3} \text{ M}$) was observed with increasing CFMS-PVP NS concentrations from 5 to $100 \mu\text{g mL}^{-1}$, which verified that the NSs are effective for GSH depletion. Electron spin resonance (ESR) spectroscopy was applied to detect $\cdot\text{OH}$ generated in situ, using 5, 5-dimethyl-1-pyrroline-N-oxide (DMPO) as the probe (Figure 2H). ESR signals could barely be observed for $\text{Co}_2\text{Fe}_{0.75}\text{Mn}_{0.25}\text{S}_6$ -PVP NSs + H_2O_2 at neutral pH conditions (pH 7.4), while increased ESR signal intensity was noted in mildly acidic conditions (pH 6.5). This reveals specificity of the CFMS-PVP NSs, in terms of their generating radicals only in the mildly acidic tumor microenvironment. Much more intense $\cdot\text{OH}$ peaks can be detected at elevated temperature (318 K), suggesting an increased temperature accelerates the Fenton reaction and generates larger amounts of $\cdot\text{OH}$. After reaction with GSH, the $\text{Co}_2\text{Fe}_{0.75}\text{Mn}_{0.25}\text{S}_6$ -PVP NSs retain their lamellar morphology. However, partial decomposition of the NSs can be observed in terms of a reduced hydrodynamic particle size ($75.7 \pm 8.7 \text{ nm}$, Figure S16, Supporting Information). XPS was utilized to study the change in valence state of Mn, Co and Fe

in CFMS-PVP NSs after treatment with GSH. The oxidation states of Co and Fe remain unchanged, but most of $\text{Mn}^{3+}/\text{Mn}^{4+}$ has been reduced to Mn^{2+} . This is clear from the presence of a typical Mn^{2+} satellite peak ($\approx 647.0 \text{ eV}$), which is absent for either Mn^{3+} or Mn^{4+} (Figure S17, Supporting Information).

To further investigate the occurrence of Fenton reactions, 3, 3', 5, 5'-tetramethylbenzidine (TMB) was employed for a kinetic analysis.^[18] The changes in absorbance occurring upon the addition of H_2O_2 ($0.05, 0.1, 0.2, 0.5, 1.0, \text{ and } 2.0 \times 10^{-3} \text{ M}$) to a suspension of $\text{Co}_2\text{Fe}_{0.75}\text{Mn}_{0.25}\text{S}_6$ -PVP NSs ($50 \mu\text{g mL}^{-1}$) are depicted in Figure S18 (Supporting Information). The corresponding initial velocities (V_0) were calculated via the Beer–Lambert law. A range of initial velocities were then fitted with the Michaelis–Menten equation and a linear double reciprocal plot (Lineweaver–Burk plot) constructed to obtain the Michaelis–Menten constant (K_m) and maximum velocity (V_{max}) (experimental details and the calculation procedure are given in the Experimental Section). The K_m and V_{max} values were calculated to be $0.46 \times 10^{-3} \text{ M}$ and $2.74 \times 10^{-8} \text{ M s}^{-1}$ for the CFMS-PVP NSs at 298 K (Figure S18A–C, Supporting Information). When the temperature was increased temperature to 318 K, the K_m and V_{max} values obtained are $0.26 \times 10^{-3} \text{ M}$ and $3.77 \times 10^{-8} \text{ M s}^{-1}$ (Figure S18D–F, Supporting Information), confirming that heat produced from the CFMS-PVP NSs could accelerate the generation of $\cdot\text{OH}$.

2.3. In Vitro Biocompatibility and PTT/CDT Study

Prior to investigating the anticancer effect of the $\text{Co}_2\text{Fe}_{0.75}\text{Mn}_{0.25}\text{S}_6$ -PVP NSs, a biocompatibility evaluation was conducted on HepG2, HeLa, and U87mg cell lines. No obvious toxicity was observed even at a concentration up to $200 \mu\text{g mL}^{-1}$, which indicates the CFMS-PVP NSs have good biocompatibility (Figure S19, Supporting Information). The survival rate of HepG2 cells also remains unchanged upon the addition of H_2O_2 , even at $100 \times 10^{-6} \text{ M}$ (Figure 3A). Subsequently, in vitro CDT induced by CFMS-PVP NSs was investigated. After incubation with $200 \mu\text{g mL}^{-1}$ of CFMS-PVP NSs and $100 \times 10^{-6} \text{ M}$ H_2O_2 for 24 h, cell viabilities of 32.7% and 82.7% were obtained at pH 6.5 and pH 7.4 respectively (Figure 3B).

To explore the ability of the $\text{Co}_2\text{Fe}_{0.75}\text{Mn}_{0.25}\text{S}_6$ -PVP NSs in combined PTT/CDT, HepG2 cells were incubated with the NSs (at $5\text{--}30 \mu\text{g mL}^{-1}$) for 24 h and then irradiated with a 808 nm laser (1.0 W cm^{-2}) for 8 min. Without H_2O_2 , the PTT efficacy of CFMS-PVP NSs was investigated, and the cell viability of 29.8% was obtained at the concentration of $30 \mu\text{g mL}^{-1}$ (Figure S20, Supporting information). In the presence of $30 \mu\text{g mL}^{-1}$ of $\text{Co}_2\text{Fe}_{0.75}\text{Mn}_{0.25}\text{S}_6$ -PVP NSs and H_2O_2 ($100 \times 10^{-6} \text{ M}$), cell viability was 12.5% and 25.4% at pH 6.5 and pH 7.4, indicating a synergistic effect from PTT/CDT (Figure 3C). To further probe the synergistic effects, the half-maximal inhibitory concentrations (IC_{50}) of CFMS-PVP NSs was calculated to obtain the combination index (CI).^[19] The CI value is less than 1.0, indicating an excellent synergistic effect of PTT/CDT.

The production of $\cdot\text{OH}$ in the HepG2 cellular environment was proven using the intracellular ROS probe 2, 7-dichlorofluorescein diacetate (DCFH-DA). Compared with the control group, HepG2 cells incubated with CFMS-PVP NSs

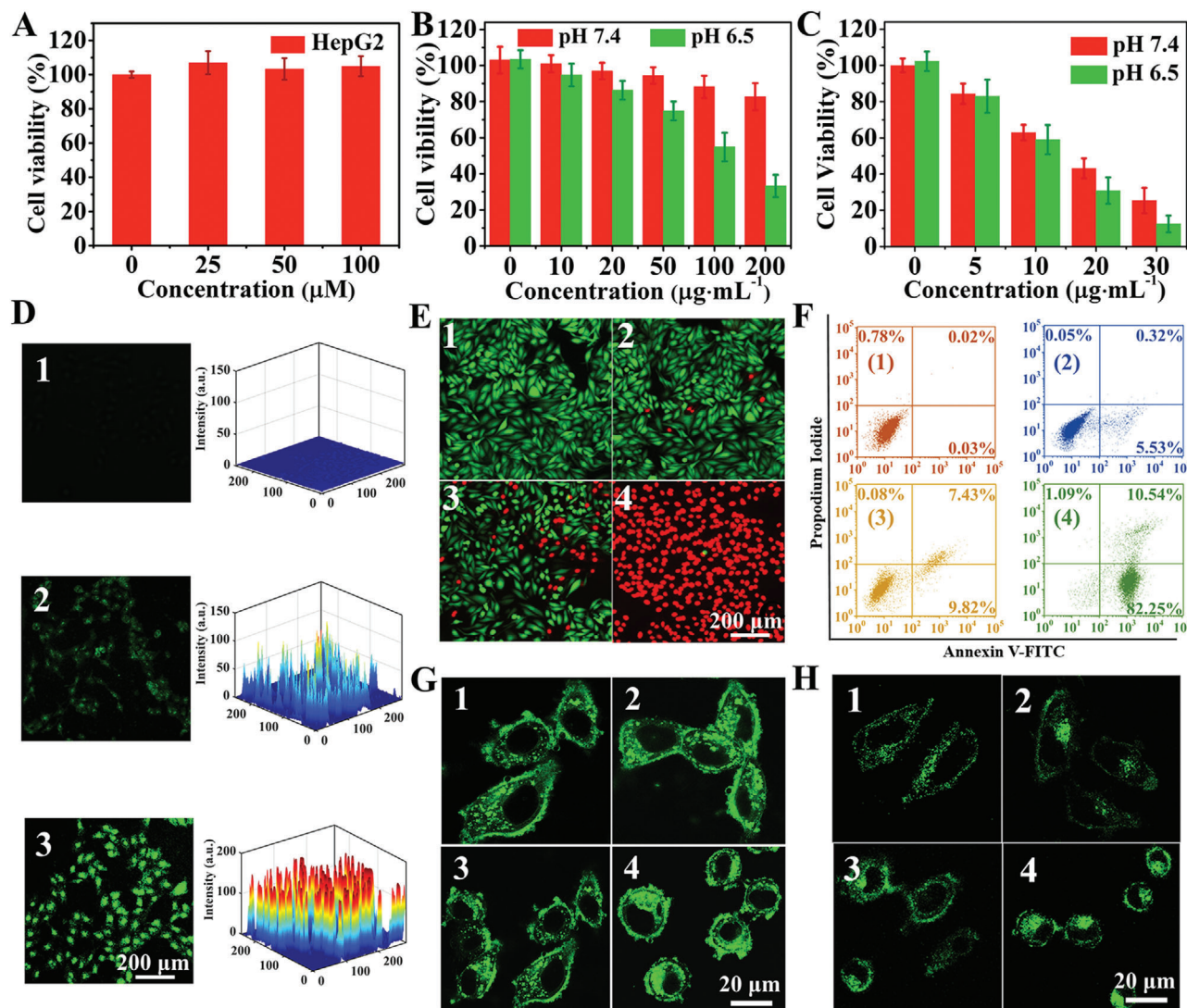


Figure 3. In vitro PTT/CDT studies with HepG2 cells. Relative viabilities of HepG2 cells are shown after incubation A) with different concentrations of H_2O_2 , and B,C) with $\text{Co}_2\text{Fe}_{0.75}\text{Mn}_{0.25}\text{S}_6$ -PVP NSs and H_2O_2 (100×10^{-6} M) at different pH values, with (B) and without (C) 808 nm laser irradiation at 1.0 W cm^{-2} for 8 min. D) Confocal images of DCFH-DA (2, 7-dichlorofluorescein diacetate) stained cells. E) Viability of cells in the presence of the CFMS-PVP NSs. F) Cell apoptosis analysis using the Annexin V-FITC/PI double staining method: 1) PBS; 2) pH 7.4 + H_2O_2 (100×10^{-6} M); 3) pH 6.5 + H_2O_2 (100×10^{-6} M); 4) pH 6.5 + H_2O_2 (100×10^{-6} M) + NIR (1.0 W cm^{-2} , 8 min). Confocal laser scanning microscope (CLSM) images of (G) LysoTracker Green DND-26 (green) stained lysosomes and (H) MitoTracker Green FM (green) stained mitochondria. Numbered panels correspond to the following treatments: 1) PBS; 2) pH 7.4 + H_2O_2 (100×10^{-6} M); 3) pH 6.5 + H_2O_2 (100×10^{-6} M); 4) pH 6.5 + H_2O_2 (100×10^{-6} M) + NIR (1.0 W cm^{-2} , 8 min).

give a weak green fluorescence signal at pH 7.4. Notably enhanced green emission was observed at pH 6.5, demonstrating that a large amount of intracellular $\cdot\text{OH}$ was produced (Figure 3D). Moreover, HepG2 cells treated with saline, and $\text{Co}_2\text{Fe}_{0.75}\text{Mn}_{0.25}\text{S}_6$ -PVP NSs with 808 nm irradiation were stained with calcein-AM and propidium iodide (PI) (Figure 3E). The results concur with the cytotoxicity data above. When the treated HepG2 cells were stained with Annexin V-FITC/PI and analyzed by flow cytometry to monitor cell apoptosis,^[20] 92.8% apoptosis was observed in HepG2 cells treated with CFMS-PVP NSs and exposed to 8 min of irradiation. Significant early-stage apoptosis appeared in the $\text{PI}^+/\text{Annexin V-FITC}^+$ region, demon-

strating effective PTT/CDT is induced by the CFMS-PVP NSs (Figure 3F).

Cell apoptosis usually originates from injury of subcellular organelle structures, including lysosomes, mitochondria, etc.^[21] We thus examined the influence of PTT/CDT on the lysosomes (Figure 3G). Compared with untreated groups and cells exposed to CFMS-PVP NSs alone, the green spotted lysosomes in the cells partially accumulated in the cytoplasm and the morphology of the cells changed somewhat in the presence of $\text{Co}_2\text{Fe}_{0.75}\text{Mn}_{0.25}\text{S}_6$ -PVP NSs and H_2O_2 at pH 6.5. After exposure to the 808 nm laser, the green spots accumulated and the intensity of the fluorescence signal increased in almost the entire cytosol, implying

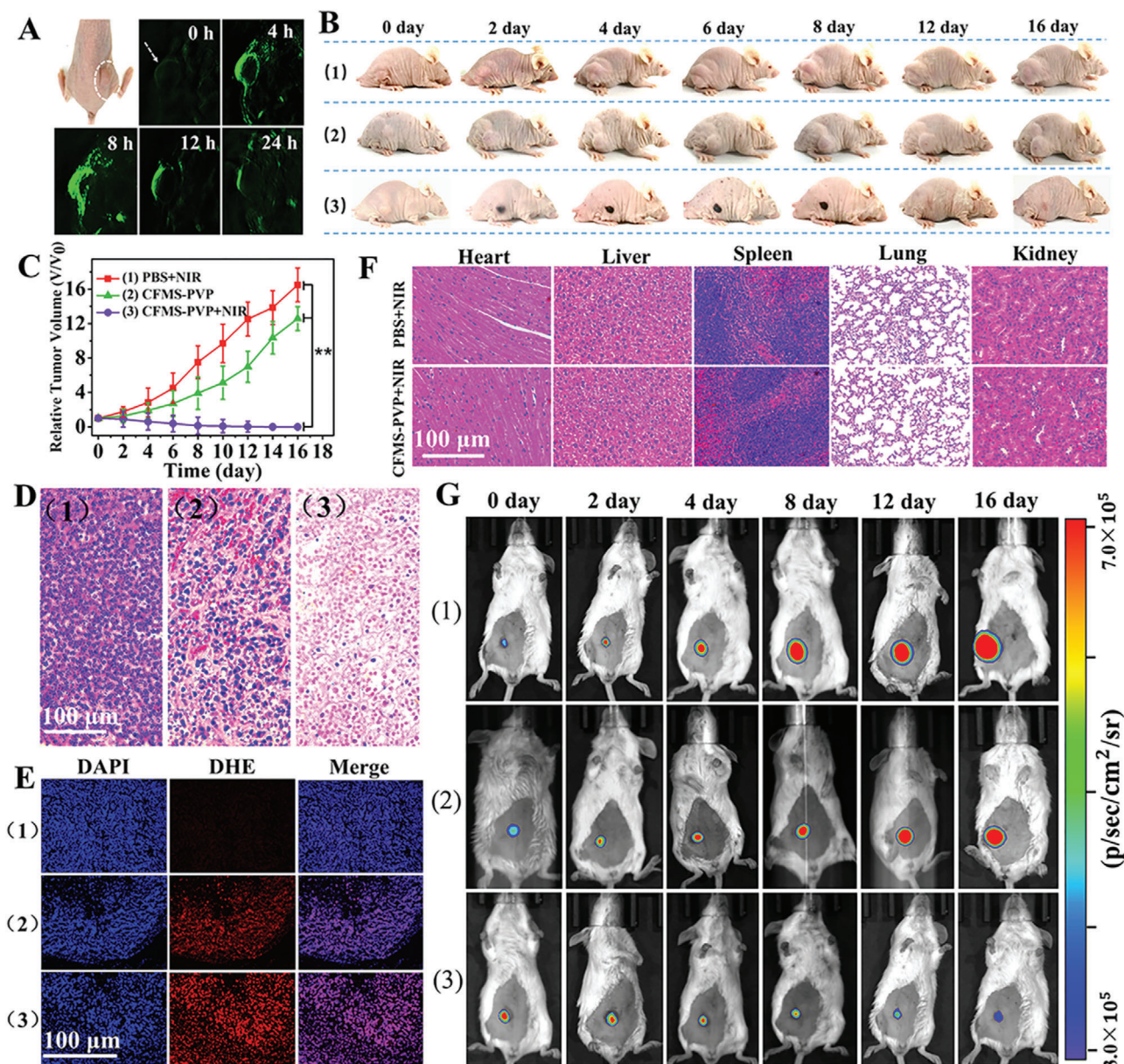


Figure 4. In vivo results in tumor-bearing mice. Treatment groups are: 1) PBS + NIR, 2) CFMS-PVP NSs, 3) CFMS-PVP NSs + NIR. A) Multispectral optical tomography system (MSOT) images of tumors tissue (arrows) at different time points after injection via the tail vein. B) Digital photographs. C) Relative tumor volumes ($n = 6$, mean \pm S.D.). D) H&E-stained histological images of the tumor site. E) H&E-stained histological images of the major organs. F) Fluorescence images of tumor slices after DHE staining (red). The nuclei were stained with DAPI (blue). G) Bioluminescence imaging of 4T1-Fluc-tumor-bearing mice. P values were calculated by ANOVA followed by Tukey's post-test ($*P < 0.05$, $**P < 0.01$).

that the CFMS-PVP NSs can destroy lysosomes and result in lysosomal membrane permeabilization. We further explored the effects of the different treatments on the mitochondria (Figure 3H). When cells were treated with CFMS-PVP NSs and H_2O_2 at pH 6.5, the mitochondria became partially fragmented due to $\cdot OH$ production. Mitochondrial fragmentation increased greatly after $Co_2Fe_{0.75}Mn_{0.25}S_6$ -PVP NSs incubation plus laser irradiation, demonstrating severe damage to mitochondria. It is concluded that local hyperthermia and $\cdot OH$ from CFMS-PVP NSs induce mitochondrial dysfunction and contribute to apoptosis.

2.4. In Vivo Anti-Tumor Therapy

Encouraged by the in vitro results, therapeutic efficacy in vivo was evaluated in HepG2 tumor-bearing mice via intravenous (i.v.) injections ($200 \mu L$, 10 mg kg^{-1}). We first assessed the PA performance of $Co_2Fe_{0.75}Mn_{0.25}S_6$ -PVP NSs in the HepG2 tumor-bearing model ($n = 3$ mice/group). As shown in Figure 4A, no PA signal was found in the tumor area (white arrow) before injection, but a distinct PA signal clearly distinguishable from the background began to appear after 4 h and reached a peak 8 h after

i.v. injection. The PA signal then decreased rapidly and became undetectable 24 h post-injection.

Subsequently, mice were randomly divided into three groups: 1) PBS + NIR (6 min irradiation, control group), 2) CFMS-PVP NSs (CDT alone), 3) CFMS-PVP NSs + NIR (6 min irradiation, PTT/CDT). 8 h after i.v. administration, in groups (1) and (3) the mice were anesthetized and then exposed to a 808 nm laser (1.0 W cm^{-2}). In vivo photothermal images to visualize temperature changes were recorded using a thermal infrared imaging device (Figure S21, Supporting Information). Compared with the PBS group, the tumor-site temperature of mice injected with $\text{Co}_2\text{Fe}_{0.75}\text{Mn}_{0.25}\text{S}_6$ -PVP NSs increased rapidly from 34.3 to 54.2 °C over 6 min (Figure S22, Supporting Information). Digital photos and the tumor volume were recorded every other day for 16 days after PTT/CDT treatment. The PBS groups show rapid tumor growth, while treatment with $\text{Co}_2\text{Fe}_{0.75}\text{Mn}_{0.25}\text{S}_6$ -PVP NSs but without NIR irradiation partially inhibits the tumor growth as a result of CDT. For mice receiving both CFMS-PVP NSs and irradiation, the tumors were completely ablated during the experimental period (Figure 4B,C). Figure S23 (Supporting Information) displays the excised tumors obtained when the mice were sacrificed after 16 days. These are consistent with the tumor volume curves measured in vivo.

Tumor tissue slices collected from three groups were stained with hematoxylin and eosin (H&E) (Figure 4D). Very clear necrosis of the HepG2 cells was observed in the $\text{Co}_2\text{Fe}_{0.75}\text{Mn}_{0.25}\text{S}_6$ -PVP NSs + NIR group, while the PBS + NIR group retained a normal cell morphology and the CFMS-PVP NSs group showed partial necrosis. To verify $\cdot\text{OH}$ production in tumors as a result of the presence of the CFMS-PVP NSs, DHE was used to detect its generation in vivo. No obvious red fluorescence was observed with PBS + NIR, while red fluorescence was visible in the CFMS-PVP NSs group. The fluorescence intensity became stronger when the NSs were administered with NIR irradiation, confirming photothermal-enhanced CDT (Figure 4E).

The Co concentrations in the major organs and tumor sites were measured by ICP to investigate in vivo accumulation and metabolism of the CFMS-PVP NSs (Figure S24A, Supporting Information). A high level of Co was observed at the tumor site as well as in most organs in the first 8 h, but then declined gradually to a low level at 48 h, demonstrating efficient degradation or excretion of the NSs. A high level of Co was detected in both urine and feces, especially in the first 8 h (Figure S24B, Supporting Information), which indicates the CFMS-PVP NSs can be excreted through the liver and kidney. After 48 h, again the Co concentrations had markedly declined. These results indicate good in vivo biocompatibility, which was further supported by H&E staining analysis of the major organs (i.e., heart, liver, spleen, lung, kidney; Figure 4F). No significant differences are observed between the CFMS-PVP NSs and PBS groups. Furthermore, no change in body-weight is seen throughout the experimental period (Figure S25, Supporting Information), indicating that all treatments had negligible off-target side effects. After mice were treated with the CFMS-PVP NSs, their blood biochemistry indices (WBC, RBC, PLT, and HGB) and levels of liver and kidney function indices (AST, ALT, BUN and CRE) did not differ from those recorded with healthy mice, again consistent with there being negligible side effect of CFMS-PVP NSs administration (Figure S26, Supporting Information).

A second in situ tumor model was developed using 4T1 tumor cells labeled with firefly luciferase. Bioluminescence imaging was used to investigate the antitumor performance of CFMS-PVP NSs through the specific binding of firefly luciferase and fluorescein. This allows rapid, sensitive and noninvasive in vivo detection as well as quantitative analysis of tumor growth and metastasis.^[22] As shown in Figure 4G and Figure S27 (Supporting Information), tumors grew rapidly in the PBS control group, while treatment with CFMS-PVP NSs partly suppressed growth. In contrast, application of CFMS-PVP NSs and exposure to 808 nm laser irradiation led to complete tumor destruction and atrophy. These results all confirm that the CFMS-PVP NSs have excellent and synergistic PTT/CDT performance, and thus potential clinical applications.

3. Conclusion

A highly tunable CFMS-PVP NSs platform was fabricated based on the vulcanization of a lamellar CoFeMn-LDH precursor. The NSs allow effective PA imaging and synergistic PTT/CDT therapy. Outstanding therapeutic outcomes are observed in vivo, arising from the excellent PCE ($\eta = 89.0\%$) and multi-functionality of the CFMS-PVP NSs. The presence of Co and Fe causes conversion of H_2O_2 overexpressed in tumor cells into toxic $\cdot\text{OH}$, and the Mn reduces intracellular GSH. The temperature rise elicited by NIR laser irradiation further accelerated the disproportionation of H_2O_2 , giving PTT-enhanced CDT. Both in vitro and in vivo therapeutic efficacy tests demonstrate inhibition of HepG2 cell proliferation, and complete eradication of tumors can be caused by the combined PTT/CDT effects of the CFMS-PVP NSs. Therefore, the ternary-metal CFMS-PVP NSs synthesized here hold great promise for future clinical cancer theranostics.

4. Experimental Section

Materials: Cobalt nitrate ($\text{Co}(\text{NO}_3)_2 \cdot 6\text{H}_2\text{O}$), iron nitrate ($\text{Fe}(\text{NO}_3)_3 \cdot 9\text{H}_2\text{O}$), magnesium nitrate ($\text{Mn}(\text{NO}_3)_2$, 50% W/W), sodium hydroxide (NaOH), sodium nitrate (NaNO_3), formamide, hydrogen peroxide solution (H_2O_2 , 30%), 5, 5-dithiobis-(2-nitrobenzoic acid) (DTNB), polyvinyl pyrrolidone (PVP, MW = 10 000), and thioacetamide (TAA) were purchased from Aladdin Chemical. Co. Ltd (Shanghai, China). 2, 7-dichlorodihydrofluorescein diacetate (DCFH-DA), calceinacetoxymethyl ester (Calcein-AM) and propidium iodide (PI) were purchased from Sigma-Aldrich (St. Louis, MO, USA). Dulbecco's modified Eagles medium (DMEM), 0.25% trypsin-EDTA and penicillin/streptomycin were obtained from Gibco (Invitrogen, Carlsbad, CA). Fetal bovine serum (FBS) was purchased from Excell Bio. Co., Ltd. (Shanghai, China). An Annexin V-FITC & propidium iodide apoptosis detection kit was purchased from Solarbio Science and Technology Co, Ltd (Beijing, China). Mito-Tracker Green and Lyso-Tracker Green were purchased from Beyotime (Beijing, China). Ultrapure water from a Milli-Q Millipore system was used in all processes. All chemicals were of analytical-grade and obtained from commercial sources, and were used without any further purification.

Preparation of CoFeMn-LDH Precursor: The synthesis of CoFeMn-LDH precursor with varying $\text{Co}_x\text{Mn}_y\text{Fe}_{1-x-y}$ was performed using a bottom-up method previously reported by the group, with some modifications. In a typical procedure, solution A was prepared from $\text{Co}(\text{NO}_3)_2 \cdot 6\text{H}_2\text{O}$ (0.4 mmol), $\text{Fe}(\text{NO}_3)_3 \cdot 9\text{H}_2\text{O}$ (0.15 mmol), and $\text{Mn}(\text{NO}_3)_2$ (0.05 mmol) in deionized water (20 mL). Solution B comprised NaNO_3 (0.1 mmol) dissolved in deionized water (20 mL) containing 25% v/v formamide. A third

solution, solution C was prepared by dissolving NaOH (0.0025 mmol) in deionized water (20 mL). Solution A and solution C were then added simultaneously into solution B, with stirring at the speed of 600 rpm at 80 °C. After cooling to ambient temperature, the products were collected by centrifugation at 7000 rpm, then the samples were washed with ethanol and deionized water three times followed by dialysis (3 kDa) to remove formamide.

Preparation of CFMS NSs: The CFMS NSs were prepared using the CoFeMn-LDH precursor and thioacetamide (TAA). Briefly, TAA (0.12 mol) was first dissolved in ethanol (40 mL) in a Teflon container (100 mL), followed by the addition of the CoFeMn-LDH precursor (0.06 mol). After hydrothermal treatment at 120 °C for 12 h, the product was collected by centrifugation at 7000 rpm for 5 min and washed thoroughly with water and ethanol. The CFMS NSs were finally re-dispersed in deionized water for subsequent experiments.

Preparation of CFMS-PVP NSs: PVP (0.06 mol) was added into the CFMS solution with ultrasonication for 30 min and then stirred at 600 rpm for 8 h. The CFMS-PVP NSs were collected by centrifugation at 7000 rpm for 5 min and washed thoroughly with deionized water and ethanol three times.

Measurement of Photothermal Performance: CFMS-PVP NSs (10, 20, 30, and 50 $\mu\text{g mL}^{-1}$), LDH suspension (50 $\mu\text{g mL}^{-1}$) and pure water were individually placed in a quartz cuvette and then irradiated with a 808 nm NIR laser (1.0 W cm^{-2}) for 10 min. The temperature changes and thermal infrared images were measured by a thermal infrared imaging device (Ti450, Fluke, Everett, WA, USA). The PCE (η) can be determined from Equation (1)

$$\eta = \frac{hs(T_{\max} - T_{\text{surr}}) - Q_{\text{dis}}}{I(1 - 10^{-A_{808}})} \quad (1)$$

Where h represents the heat transfer coefficient of the CFMS-PVP NSs suspension, s is the surface area of the container, T_{\max} is the maximum temperature of the suspension, T_{surr} is the temperature of the surroundings, Q_{dis} is the heat associated with light absorbance by the solvent, I is the incident laser power (1.0 W cm^{-2}), and A_{808} is the absorbance of the CFMS-PVP NSs at 808 nm.

To get the value of hs , θ is expressed using the maximum system temperature

$$\theta = \frac{T - T_{\text{surr}}}{T_{\max} - T_{\text{surr}}} \quad (2)$$

τ_s can be derived according to Equation (3)

$$t = -\tau_s \ln \theta \quad (3)$$

Then, hs can be determined from Equation (4)

$$hs = \frac{m_D C_D}{\tau_s} \quad (4)$$

where τ_s is the time constant for the heat transfer, and m_D and C_D are the mass (1.0 g) and heat capacity (4.2 J g^{-1}) of deionized water used to disperse the CFMS-PVP NSs.

Q_{dis} represents the heat input absorbed by pure water and the quartz cuvette, and can be described as follows

$$Q_{\text{dis}} = \frac{m_D C_D (T_{\max(\text{water})} - T_{\text{surr}})}{\tau_{\text{water}}} \quad (5)$$

Where $T_{\max(\text{water})}$ is 34.6 °C, T_{surr} is 28.6 °C, τ_{water} is 356. Hence, Q_{dis} was calculated to be 0.071 W. Therefore, τ_s for heat transfer from the CFMS-PVP NSs was determined to be 292.6 s by fitting a straight line to the data from the cooling period versus $-\ln \theta$. Thus, according to Equation (4), hs was determined to be 14.35 $\text{mW } ^\circ\text{C}^{-1}$. Finally, the PCE (η) of the CFMS-PVP NSs can be calculated to be 89.0%.

Extracellular Depletion of GSH: The consumption of GSH was monitored by absorption in the DTNB assay. Solutions containing 1×10^{-3} M GSH were added to different amounts of CFMS-PVP NSs (5, 20, 50, and 100 $\mu\text{g mL}^{-1}$). The solutions (4 mL) were incubated for different times (0, 10, 20, 40, 60, 80, 100, 120, and 140 min) and then centrifuged at 10000 rpm for 10 min to remove the CFMS-PVP NSs. After 10 min of coincubation of the supernatant (2 mL) and DTNB solution (0.8×10^{-3} M, 2 mL), absorbance was recorded using a microplate reader.

OH Production: 5, 5-dimethyl-1-pyrroline N-oxide (DMPO) was used as a $\cdot\text{OH}$ trapping agent. Reaction groups were established as follows: 1) 20 $\mu\text{L H}_2\text{O}_2$ (5×10^{-3} M) + 1 $\mu\text{g CFMS-PVP NSs}$ at pH 7.4; 2) 20 $\mu\text{L H}_2\text{O}_2$ at pH 6.5; 3) 1 $\mu\text{g CFMS-PVP NSs}$ at pH 6.5; 4) 20 $\mu\text{L H}_2\text{O}_2$ + 1 $\mu\text{g CFMS-PVP NSs}$ at pH 6.5, and 5) 20 $\mu\text{L H}_2\text{O}_2$ + 1 $\mu\text{g CFMS-PVP NSs}$ with 5 min heating using 318 K water bath at pH 6.5. Subsequently, 400 μL of DMPO buffer solution (100×10^{-3} M) and each reaction mixture were added to a quartz capillary, and X-band EPR spectra were measured in perpendicular mode on a Bruker (Germany) EMX-500 10/12 spectrometer with the following settings: microwave frequency = 9.872 GHz, microwave power = 6.375 mW, modulation frequency = 100.00 kHz and modulation amplitude = 1.00 G.

Michaelis–Menten Kinetics: The Fenton performance of CFMS-PVP NSs was studied by monitoring the absorption spectra of TMB at 652 nm using a microplate reader. In a typical test, CFMS-PVP NSs (final concentration 50 $\mu\text{g mL}^{-1}$), TMB (final concentration 800×10^{-6} M) and varied concentrations of H_2O_2 (0.05, 0.10, 0.20, 0.50, 1.0, and 2.0×10^{-3} M) were suspended in a Acetic acid-Sodium acetate (HAc-NaAc) buffer solution (pH 6.5) at controlled temperature (298 and 318 K). Then Michaelis–Menten constant was calculated according to Lineweaver–Burk plots, based on Equations (6) to (8).

$$A = Kbc \quad (6)$$

$$v_0 = \frac{V_{\max} [S]}{K_M + [S]} \quad (7)$$

$$\frac{1}{v_0} = \frac{K_M}{V_{\max}} \frac{1}{[S]} + \frac{1}{V_{\max}} \quad (8)$$

Where A is absorbance of TMB at 652 nm, K represents the molar absorption coefficient, b is the thickness of the container, c is the concentration of TMB, v_0 is the initial velocity, V_{\max} represents the maximum reaction velocity, S is the substrate concentration, and K_m expresses the Michael constant.

In Vitro PA Imaging: In vitro PA imaging was performed on a multi-spectral optical tomography system (MSOT inVision 256, iThera 8 Medical, Germany). CFMS-PVP NSs aqueous suspension at different concentrations (2.5, 5, 10, 20, and 50 $\mu\text{g mL}^{-1}$, 1 mL) were placed in agar gel cylinders for in vitro PA imaging.

Cell Culture: HepG2, U87mg, and HeLa cell lines obtained from Basic Medical Sciences Chinese Academy of Medical Sciences (Beijing, China) were cultured in DMEM supplemented with 10% v/v fetal bovine serum (FBS), 1% streptomycin and penicillin (v/v, Corning, USA) under a humidified atmosphere of 5% CO_2 at 37 °C.

In Vitro Cytotoxicity: For cell viability studies, HepG2, U87mg, and HeLa cells were seeded in 96-well plates (1×10^4 cells per well, in 200 μL of medium) for 24 h. Then the culture medium was replaced by fresh culture medium containing CFMS-PVP NSs at different concentrations (0, 10, 20, 50, 100, 200 $\mu\text{g mL}^{-1}$, 200 μL). After incubation of 24 h and thorough washing with PBS, the cell viability was determined by the 3-[4, 5-dimethylthiazol-2-yl]-2, 5-diphenyltetrazolium bromide (MTT) assay.

In Vitro CDT Measurement: HepG2 cells were seeded in 96-well plates (1×10^4 cells per well, 200 μL) for 24 h. The pH of the media was adjusted (7.4 and 6.5) to simulate the extracellular microenvironment in a solid tumor. HepG2 cells were incubated with fresh medium (pH 7.4 and pH 6.5) containing 100×10^{-6} M H_2O_2 and CFMS-PVP NSs at concentrations of 10, 20, 30, 50, 100, and 200 $\mu\text{g mL}^{-1}$ (200 μL per well) for another 24 h. The cell viability was measured by the MTT assay.

In Vitro Synergistic CDT and PTT: HepG2 cells were seeded in 96-well plates at a density of 1×10^4 cells per well (200 μ L) for 24 h. Then the culture medium was replaced by fresh culture medium containing CFMS-PVP NSs at different concentrations (2.5, 5, 10, 20, and 30 μ g mL⁻¹, 200 μ L per well) at the same time, and further co-incubated for 12 h, cells were irradiated with 808 nm NIR light (1.0 W cm⁻²) for 10 min. The MTT assay was used to evaluate the cytotoxicity of the various treatments after another 12 h. To verify the MTT results, Calcein-AM/PI was used to stain living and dead cells according to the manufacturer's instructions.

Detection of Intracellular ·OH Production: The DCFH-DA fluorescent probe was used to detect intracellular ·OH. HepG2 cells were seeded into 12-well culture dishes (1×10^5 cells per well, in 200 μ L of medium) for 24 h (37 °C, 5% CO₂). Then, different treatments (PBS, H₂O₂ with CFMS-PVP NSs at pH 7.4 and pH 6.5) were applied to the cells for 12 h. Subsequently the cells were washed several times with PBS and DCFH-DA solution (0.2×10^{-6} M, 1 mL per well) was added to the cells for another 60 min. The presence of intracellular ·OH was examined by the fluorescence of DCFH ($\lambda_{\text{ex}} = 488$ nm, $\lambda_{\text{em}} = 525$ nm).

Assessing the Effect of PTT/CDT on Lysosomes and Mitochondria: For the lysosomes damage study, HepG2 cells (1×10^5 cells per dish, 3 mL) were cultured in 35 mm glass-bottom culture dishes for 24 h. Next, the cells were cultured with DMEM, CFMS-PVP NSs (30 μ g mL⁻¹, with the addition of H₂O₂ at pH 6.5), CFMS-PVP NSs (NIR 8 min) for another 24 h. The cells were subsequently incubated with LysoTracker Green DND-26 (200 μ L, 50×10^{-9} M) at 37 °C for 15 min in serum-free DMEM. After washing with PBS three times, the serum-free DMEM was added to the dishes, and the cells were visualized by CLSM. For the mitochondria damage study, cell culture was performed using the same protocol.

Animal Model: Healthy male Balb/c mice (ages 5–6 weeks old) were purchased from Beijing Vital River Laboratory Animal Technology Co., Ltd (Beijing, China). The animal procedures followed the protocols approved by the Animal Care and Use Committee of Peking Union Medical College Hospital. HepG2 cells (1×10^7 cells dissolved in 100 μ L PBS) were implanted subcutaneously into the mice to construct the tumor models. The tumor size was measured by a caliper every two days with 16 days' treatment. Mice with tumor sizes of 70 mm³ were selected for experimental studies.

PA Imaging: CFMS-PVP NS suspension (1 mg mL⁻¹, 200 μ L) were i.v. injected into the tumor-bearing mice, and PA signals were recorded at 0, 4, 8, 12, and 24 h post-injection under varied excitation wavelengths (680–900 nm) using a multispectral optical tomography system (MSOT inVision 256, iThera 8 Medical, Germany).

In Vivo Toxicity Study: HepG2 tumor-bearing mice were randomly divided into three groups (6 animals per group): 1) saline (control group), 2) CFMS-PVP NSs (CDT group), and 3) CFMS-PVP NSs + 808 nm laser (PTT/CDT group). 200 μ L of CFMS-PVP NS suspension (1 mg kg⁻¹) was i.v. injected into tumor-bearing mice. 8 h post-injection, for the laser groups the tumor area was irradiated with a 808 nm laser (1.0 W cm⁻²) for 6 min. Real-time temperature changes and thermal images were recorded using a thermal infrared imaging device. The tumor sizes and mice body weights were recorded every other day and the tumor volume was calculated using the following formula

$$\text{Volume} = \text{Tumor length} \times \frac{\text{Tumor width}^2}{2} \quad (9)$$

Histology: Mice were sacrificed on day 16, and the tumors and major organs were excised and fixed in 4% formalin for histology analysis. The tissues were subject to hematoxylin and eosin (H&E) staining using standard protocols and observed under a digital microscope (Leica DM6000M).

ICP Determination: To study the biodistribution of CFMS-PVP NSs in Balb/c mice, 200 μ L of a CFMS-PVP NS suspension (1 mg mL⁻¹) was i.v. injected into tumor-bearing mice. The mice were sacrificed after 0, 4, 8, 12, and 24 h post-administration. The organs and excrement were collected, dissected, weighed and digested by nitric acid for distribution studies and ICP (Shimadzu ICPS-7500) was used to measure the Co concentration.

Establishment of a 4T1-Fluc Tumor Orthotopic Mouse Model: Animals were obtained from Beijing Vital River Laboratory Animal Technology Co.,

Ltd. (Beijing, China). The animal procedures were carried out in compliance with the protocols approved by Animal Care and Use Committee of Peking Union Medical College Hospital. For orthotopic tumor implantation, a mixture of 4T1 cells (5×10^6 , 100 μ L in PBS) labeled with Firefly luciferase was injected into the abdomen of mice. Mice with tumor volumes of around 70 mm³ were used for experiments.

In Vivo Bioluminescence Imaging: 4T1-Fluc tumor-bearing mice were randomly allocated to three different groups (4 mice per group): 1) saline (control group), 2) CFMS-PVP NSs (CDT group), and 3) CFMS-PVP NSs with 808 nm NIR irradiation (PTT/CDT group). 200 μ L of the NS suspension at 1 mg mL⁻¹ total dose or an equivalent volume of saline were i.v. injected. 8 h post-injection, the tumor area was irradiated with a 808 nm laser (1.0 W cm⁻²) for 6 min. To monitor tumor growth, the D-Luciferin probe (150 mg kg⁻¹) was intraperitoneally injected into the mice, then mice were anesthetized through isoflurane inhalation (2–3%) for 5 min. Then animals were imaged with the IVIS Lumina fluorescence imaging system every other day.

Statistical Analysis: Data are expressed as mean \pm standard deviation (S.D). Statistical comparisons were made by unpaired Student's *t*-test (between two groups) and one-way ANOVA (for multiple comparisons) followed by Tukey's post-test: **p* < 0.05, ***p* < 0.01.

Data Availability: The data that support the findings of this study are available from the corresponding author on reasonable request.

Supporting Information

Supporting Information is available from the Wiley Online Library or from the author.

Acknowledgements

Y.Z. and Y.W. contributed equally to this work. This work was supported by the National Natural Science Foundation of China (NSFC: 21971007, 21671013, 21601010, 21521005) and the Fundamental Research Funds for the Central Universities (buctylkxj01, XK1802-6, XK1803-05).

Conflict of Interest

The authors declare no conflict of interest.

Keywords

layered double hydroxide, synergistic therapy, topotactic transformation, transition metal dichalcogenides

Received: January 21, 2020

Revised: June 2, 2020

Published online:

- [1] a) X. Huang, Z. Zeng, H. Zhang, *Chem. Soc. Rev.* **2013**, *42*, 1934; b) H. Li, Y. Li, A. Aljarb, Y. Shi, L. J. Li, *Chem. Rev.* **2017**, *118*, 6134; c) S. Zhu, L. Gong, J. Xie, Z. Gu, Y. Zhao, *Small Methods* **2017**, *1*, 1700220; d) H. Zhao, Q. Guo, F. Xia, H. Wang, *Nanophotonics* **2015**, *4*, 128.
- [2] a) X. Zhu, X. Ji, N. Kong, Y. Chen, M. Mahmoudi, X. Xu, T. Gan, *ACS Nano* **2018**, *12*, 2922; b) Y. Liu, P. Bhattarai, Z. Dai, X. Chen, *Chem. Soc. Rev.* **2019**, *48*, 2053; c) J. Hao, G. Song, T. Liu, X. Yi, K. Yang, L. Cheng, Z. Liu, *Adv. Sci.* **2017**, *4*, 1600160.

- [3] a) T. H. Yang, K. C. Chiu, Y. W. Harn, H. Y. Chen, R. F. Cai, J. J. Shyue, Y. H. Lee, *Adv. Funct. Mater.* **2017**, *28*, 1706113; b) X. Lin, Y. Liu, K. Wang, C. Wei, W. Zhang, Y. Yan, Y. S. Zhao, *ACS Nano* **2018**, *12*, 689; c) C. Martella, C. Mennucci, A. Lamperti, E. Cappelluti, F. B. de Mongeot, A. Molle, *Adv. Mater.* **2018**, *30*, 1705615.
- [4] a) X. J. Wu, X. Huang, X. Qi, H. Li, B. Li, H. Zhang, *Angew. Chem., Int. Ed.* **2019**, *53*, 8929; b) Y. Chen, Z. Fan, Z. Zhang, W. Niu, C. Li, N. Yang, H. Zhang, *Chem. Rev.* **2018**, *118*, 6409.
- [5] a) Z. Tang, H. Zhang, Y. Liu, D. Ni, H. Zhang, J. Zhang, W. Bu, *Adv. Mater.* **2017**, *29*, 1701683; b) Z. Meng, F. Wei, W. Ma, N. Yu, P. Wei, Z. Wang, M. Zhu, *Adv. Funct. Mater.* **2016**, *26*, 8231; c) W. Yang, W. Guo, W. Le, G. Lv, F. Zhang, L. Shi, B. Zhang, *ACS Nano* **2016**, *10*, 10245.
- [6] a) S. Gao, H. Lin, H. Zhang, H. Yao, Y. Chen, J. Shi, *Adv. Sci.* **2019**, *6*, 1801733; b) M. Xing, W. Xu, C. Dong, Y. Bai, J. Zeng, Y. Zhou, Y. Yin, *Chem* **2018**, *4*, 1359; c) H. Lin, Y. Chen, J. Shi, *Chem. Soc. Rev.* **2018**, *47*, 1938; d) S. Gao, Y. Jin, K. Ge, Z. Li, H. Liu, X. Dai, Y. Zhang, S. Chen, X. Liang, J. Zhang, *Adv. Sci.* **2019**, *6*, 1902137.
- [7] a) L. S. Lin, J. Song, L. Song, K. Ke, Y. Liu, Z. Zhou, G. Niu, *Angew. Chem., Int. Ed.* **2018**, *57*, 4902; b) X. H. Lin, S. Y. Liu, X. Zhang, R. Zhu, S. Chen, X. Chen, J. B. Song, H. Yang, *Angew. Chem., Int. Ed.* **2019**, *58*, 2.
- [8] a) B. Yang, Y. Chen, J. Shi, *Adv. Mater.* **2019**, *31*, 1901778; b) Z. Dong, L. Feng, Y. Chao, Y. Hao, M. Chen, F. Gong, Z. Liu, *Nano Lett.* **2018**, *19*, 805.
- [9] X. Li, X. Huang, S. Xi, S. Miao, J. Ding, W. Cai, J. Wang, *J. Am. Chem. Soc.* **2018**, *140*, 12469.
- [10] a) X. Mei, J. Ma, X. Bai, X. Zhang, S. Zhang, R. Liang, X. Duan, *Chem. Sci.* **2018**, *9*, 5630; b) P. Li, M. Wang, X. Duan, L. Zheng, X. Cheng, Y. Zhang, W. Liu, *Nat. Commun.* **2019**, *10*, 1711.
- [11] a) Y. Yang, X. Yang, X. Fang, K. Wang, D. Yan, *Adv. Sci.* **2018**, *5*, 1801187; b) M. Arif, G. Yasin, L. Luo, W. Ye, M. A. Mushtaq, X. Fang, D. Yan, *Appl. Catal., B* **2020**, *265*, 118559; c) M. Arif, G. Yasin, M. Sha-keel, M. A. Mushtaq, W. Ye, X. Fang, D. Yan, *Mater. Chem. Front.* **2019**, *3*, 520; d) R. Gao, D. Yan, *Nano Res.* **2018**, *11*, 1883; e) R. Gao, D. Yan, *Chem. Sci.* **2017**, *8*, 590.
- [12] L. Zhou, M. Shao, C. Zhang, J. Zhao, S. He, D. Rao, X. Duan, *Adv. Mater.* **2017**, *29*, 1604080.
- [13] a) X. Long, G. Li, Z. Wang, H. Zhu, T. Zhang, S. Xiao, S. Yang, *J. Am. Chem. Soc.* **2015**, *137*, 11900; b) Y. Li, J. Yin, L. An, M. Lu, K. Sun, Y. Q. Zhao, P. Xi, *Small* **2018**, *14*, 1801070.
- [14] a) B. Li, F. Yuan, G. He, X. Han, X. Wang, J. Qin, C. Wu, *Adv. Funct. Mater.* **2017**, *27*, 1606218; b) J. Tian, H. Zhu, J. Chen, X. Zheng, X. Duan, K. Pu, P. Chen, *Small* **2017**, *13*, 22; c) X. Huang, W. Zhang, G. Guan, G. Song, R. Zou, J. Hu, *Acc. Chem. Res.* **2017**, *50*, 2529.
- [15] a) Z. Xiao, C. Xu, X. Jiang, W. Zhang, Y. Peng, R. Zou, J. Hu, *Nano Res.* **2016**, *9*, 1934; b) J. Wang, Y. Li, L. Deng, N. Wei, Y. Weng, S. Dong, T. Wu, *Adv. Mater.* **2017**, *29*, 1603730; c) X. Jiang, S. Zhang, F. Ren, L. Chen, J. Zeng, M. Zhu, Z. Li, *ACS Nano* **2017**, *11*, 5633.
- [16] a) Q. Fu, R. Zhu, J. Song, H. Yang, X. Chen, *Adv. Mater.* **2019**, *31*, 1805875; b) K. Zhang, Z. Yu, X. Meng, W. Zhao, Z. Shi, Z. Yang, X. Zhang, *Adv. Sci.* **2019**, *6*, 1900530.
- [17] a) Y. Liu, W. Zhen, L. Jin, S. Zhang, G. Sun, T. Zhang, H. Zhang, *ACS Nano* **2018**, *12*, 4886; b) Y. Liu, J. Wu, Y. Jin, W. Zhen, Y. Wang, J. Liu, Y. Yang, *Adv. Funct. Mater.* **2019**, *29*, 1904678.
- [18] C. Zhang, W. Bu, D. Ni, S. Zhang, Q. Li, Z. Yao, J. Shi, *Angew. Chem., Int. Ed.* **2016**, *55*, 2101.
- [19] a) S. Liu, Y. Guo, R. Huang, J. Li, S. Huang, Y. Kuang, C. Jiang, *Biomaterials* **2012**, *33*, 4907; b) F. Ponthan, M. Wickström, H. Gleissman, O. M. Fuskevåg, L. Segerström, B. Sveinbjörnsson, C. P. F. Redfern, S. Eksborg, P. Kogner, J. I. Johnsen, *Clin. Cancer Res.* **2007**, *13*, 1036.
- [20] R. Gao, X. Mei, D. Yan, R. Liang, M. Wei, *Nat. Commun.* **2018**, *9*, 2798.
- [21] a) J. W. Eaton, M. Qian, *Free Radical Biol. Med.* **2002**, *32*, 833; b) P. P. Lie, R. A. Nixon, *Neurobiol. Disease* **2019**, *122*, 94; c) D. Y. Zhang, Y. Zheng, C. P. Tan, J. H. Sun, W. Zhang, L. N. Ji, Z. W. Mao, *ACS Appl. Mater. Interfaces* **2017**, *9*, 6761; d) I. T. Mak, W. B. Weglicki, *J. Clin. Invest.* **1985**, *75*, 58.
- [22] a) Z. Zhao, C. Chen, W. Wu, F. Wang, L. Du, X. Zhang, J. W. Lam, *Nat. Commun.* **2019**, *10*, 768; b) C. Liu, S. Zhang, J. Li, J. Wei, K. Müllen, M. Yin, *Angew. Chem., Int. Ed.* **2019**, *58*, 1638; c) M. Zheng, Y. Liu, Y. Wang, D. Zhang, Y. Zou, W. Ruan, B. Shi, *Adv. Mater.* **2019**, *31*, 1903277; d) S. W. Chung, J. U. Choi, Y. S. Cho, H. R. Kim, T. H. Won, P. Dimitrion, Y. Byun, *Adv. Sci.* **2018**, *5*, 1800368; e) W. Song, K. Tiruthani, Y. Wang, L. Shen, M. Hu, O. Dorosheva, L. Huang, *Adv. Mater.* **2018**, *30*, 1805007.